Energy 151 (2018) 1–10

Contents lists available at ScienceDirect

Energy

journal homepage: www.elsevier.com/locate/energy

Reverse electrodialysis: Modelling and performance analysis based on multi-objective optimization

Rui Long*, Baode Li, Zhichun Liu, Wei Liu

School of Energy and Power Engineering, Huazhong University of Science and Technology, 1037 Luoyu Road, Wuhan, 430074, China

ARTICLE INFO

Article history:
Available online 2 March 2018

Keywords:
Reverse electrodialysis (RED)
Modeling
Multi-objective optimization
Power density
Energy efficiency

ABSTRACT

In this paper, we proposed a refined model to describe the RED process by considering the variation of flow rates along the flow direction, and the concentration depended density and viscosity. The model was verified by good accordance between the calculated and experimental measured data. For evaluating the performance of a RED stack for some special applications, the net power density and the energy efficiency are two main criteria. However, they could not achieve their maximum values simultaneously. To achieve such a compromise, an optimization based on Non-dominated Sorting Genetic Algorithm II (NSGA-II) was conducted. Besides, the net power output and energy efficiency under single-objective optimization methods were calculated and compared. Results revealed that compared to the results under the maximum net power density, the net power density under the multi-objective optimization is slightly less than the maximum one, meanwhile the energy efficiency was much greater. The performance under the multi-objective optimization exhibited no obvious disadvantage against that under the maximum energy efficiency, considering the significant increase of the net power density.

1. Introduction

As the fast depletion of the fossil fuels, human beings suffer much from its detrimental byproducts such as PM 2.5, which can permanently damage our breathing system along with its convenient supply of electricity and power. Such solutions have been proposed to alleviate these problems as developing new and renewable resources and reutilization of the waste thermal energy, on which much efforts have been devoted to [1–4]. Salinity gradient power generation technologies, extracting energy from different salt solutions, offer alternative and promising ways to produce electricity, considering the huge amount of sea and river water. Generally, there are three forms of salinity gradient power generation technologies: pressure retarded osmosis (PRO) [5–7], reverse electrodialysis (RED) [8–11], and capacitive mixing (CAPMIX) [12–15], among which RED systems have been extensively investigated and serve as a more appealing and potential future technology due to its relatively high efficiency and low operation pressure [16].

For studying the characteristics of the RED system, numerical simulation and experiment study are two ordinary ways to analyze the performance of the RED system. Many models have been proposed to describe the process of the RED system. The empirical formulas could provide a preliminary way to evaluate the rough performance specifications of the RED system. However they could not illustrate the mass and concentration profiles of the salty solutions with different concentrations. Based on the mass and species conservation equations, 1D models have been developed to investigate the concentration variation along the flow direction [17]. Veerman et al. [18] propose a 1D model to describe the RED process by neglecting the changes of the volume flow rate of the high concentration (HC) and low concentration (LC) solutions, and claimed that segmentation of the electrodes could be used to dramatically increase the power density. Tedesco et al. [19] presented a multi-scale mathematical model based on mass conservation and constitutive equation. Veerman et al. [20] presented a model for the ionic shortcut currents in a RED stack whose effect could be reduced via a proper stack design. As 1D model could only reflect the concentration along the flow direction, in order to analyze concentration distribution perpendicular to the flow direction, which impact the transmembrane ion transfer characteristics, models with higher dimensions by solving the strongly coupled Poisson equation, the Nernst-Planck equation, and the Navier-Stokes equations could provide a deeper sight into

* Corresponding author.
E-mail addresses: r_long@hust.edu.cn (R. Long), w_liu@hust.edu.cn (W. Liu).

https://doi.org/10.1016/j.energy.2018.03.003
0360-5442/

illustrating the concentration [21–23]. However the model could only be employed to analyze the performance with simple geometry, as the membrane properties are strongly impacted by the geometric structures, which are often determined by the experiment test. Gurreri et al. [24] used CFD to investigate the impact of geometric characteristics and operation parameters on the concentration polarization. Along with the numerical simulation, experimental investigation plays an important role in analyzing the performance of the RED systems. Pawlowski et al. [25] experimentally studied the pressure drop in the RED stack, and proposed a model to systematically describe the geometric impact on the pressure drop. Geise et al. [26] experimentally investigated the membrane resistance when the membrane was placed between solutions of different concentrations, which was the usual case in the RED systems.

Gross power density, net power density and energy efficiency are the main criteria measuring the performance of the RED stacks, which are strongly impacted by the flow rates, concentrations, membrane properties and stack configurations. Among them, the net power density of the RED stacks is mainly focused on. Zhu et al. [27] reduced pumping energy by using different flow rates of high and low concentration solutions in RED cells. Hong et al. [28] examined the effect of monovalent and multivalent ions on the power density of the RED system and found multivalent ions led to a 9–20% lower power density than monovalent ions mainly due to the higher internal stack resistance of the multivalent ions. Kim et al. [29] investigated the performance of the RED stack with anodic alumina nanopores. Güler et al. [30] researched membrane bulk properties on the RED performance in practice. Güler et al. [31] implemented the micro-structured membranes in the RED system to alleviate the use of spacers, and 20% higher net power density was achieved. Jin et al. [32] studied the performance of the RED system with nanocomposite membrane containing$Fe_2O_3 - SO_4^{2-}$, and found that 0.5–0.7 wt% $Fe_2O_3 - SO_4^{2-}$ could obviously enhance the permselectivity of the ion-exchange membranes, thus a higher power density. Vermaas et al. [33] created a profiled membrane comprising ridges on one side of the membrane to replace the spacers, and the ohmic resistance was significantly decreased. Moreover, Liu et al. [34] created hemispherical protrusions on the cation exchange membranes to decrease the microbial reverse-electrodialysis cells (MRC) stack resistance, and a 38% increase in power density was obtained. Luo et al. [35] researched different numbers of cell pairs and stack arrangements to improve the performance of the MRC.

For improving the performance of the RED system, previous literature are mainly focused on the maximum net power density. However, the energy efficiency, reflecting the degree of the energy utilization of the salt solutions, should also be included, to measure the conversion ability of the RED system, especially, for the RED based closed loop systems such as MD-RED system studied in Ref. [16] where RED is a sub system, whose efficiency plays an important role in determining the system overall efficiency. In addition, in the regions with abundant brine water, where river water is not so sufficient, the energy efficiency and power density should both be considered to economically utilize the salinity gradient energy. Furthermore, although the CFD simulation could give us deeper insight into the concentration polarization, it is not applicable for design and system optimization considering its huge computing duration. Therefore, the traditional 1D model based on mass and species conservation is still appealing due to its relatively less computing time required. However, the volume flow rate changes of the salt solutions in the RED process are rarely considered in the aforementioned literature. And considering their effects could help us better understand and investigate the performance of the RED system. In this paper, we proposed a model for the RED process by including the concentration-depended density and volume flow rate variation along the flow direction, and then conducted an optimization of the RED system with maximum net power density and energy efficiency as the objective functions based on the proposed model. Generally, the net power density and energy efficiency could not achieve their maximum values simultaneously. Many methods have been developed to coordinate the conflicting performance specifications in thermodynamic analysis, such as Non-dominated Sorting Genetic Algorithm II (NSGA-II) and multi-objective evolutionary algorithm based on decomposition (MOEA/D) [36]. Among them, NSGA-II has the advantage of less calculation demand and good convergence, which has been widely applied in optimizing thermodynamic systems with various conflicting objectives [37]. In this paper, the NSGA-II was employed to obtain the Pareto frontier coordinating the net power density and energy efficiency. As the Pareto set reflects different weights of the two objectives, the technique for order preference by similarity to an ideal solution (TOPSIS) was utilized to identify the final optimal point of the RED system. The net power density and energy efficiency of the RED system for different membranes under optimal conditions were obtained. For comparison, the gross power density, net power density, hydrodynamic loss of the RED system along the flow direction under single-objective function conditions were discussed. In addition, the average net power density, energy efficiency and energy dissipation under different optimization methods were systematically analyzed. Finally, some conclusions were drawn.

2. Model development

2.1. Maximum power output of the RED stack

As shown in Fig. 1, the conventional RED stack consists of serial repeating RED cells (N pairs). Solutions with different concentrations alternatively flow through the channels separated by the AEM and CEM. For a RED cell, the Nernst potential difference over the IEMs is calculated as [20]:

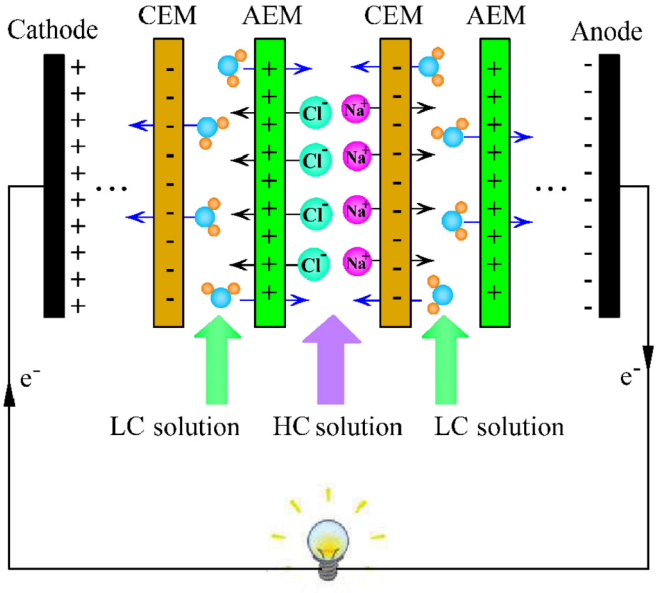

Fig. 1. Schematic diagram of reverse electrodialysis stacks.

$$E_{cell}(x) = N\left[\alpha_{CEM}\frac{RT}{F}\ln\frac{\gamma_H^{Na}(x)C_H(x)}{\gamma_L^{Na}(x)C_L(x)} + \alpha_{AEM}\frac{RT}{F}\ln\frac{\gamma_H^{Cl}(x)C_H(x)}{\gamma_L^{Cl}(x)C_L(x)}\right] \tag{1}$$

where α is the permselectivity of the membrane. γ are the activity coefficients used in thermodynamics to account for deviations from ideal behavior in a mixture of chemical substances which can be obtained by the extended Debye-Huckel equation [38]:

$$\gamma(x) = \exp\left[\frac{-0.51z^2\sqrt{I(x)}}{1+(A/305)\sqrt{I(x)}}\right] \tag{2}$$

where$I$is the ion strength of the solution and A is the effective hydrated ion radius.

The space-dependent area specific resistance $R_{a,cell}(x)$ is [20,38]:

$$R_{a,cell}(x) = N\left(\frac{f}{\Lambda_m}\left(\frac{\delta_H}{C_H(x)}+\frac{\delta_L}{C_L(x)}\right)+R_{AEM}+R_{CEM}\right)+R_{\mathrm{el}} \tag{3}$$

where $\Lambda_m$is the molar conductivity of electrolyte (NaCl) solution that measures the efficiency with which a given electrolyte conducts electricity in solution, which is impacted by the solution concentration. $\delta_H$and δ_L is the thickness of the HC and LC solution compartments. $f$is a measure for the increase of the electrical resistance due to the negative effects of the spacer. R_{AEM} and R_{CEM} are the membrane area resistance. R_{el} is the membrane area ohmic resistance of the electrodes and their compartments.

According to Ohm's law, the current density (j) is

$$j(x) = \frac{E_{cell}(x)}{R_{a,cell}(x)+R_{a,ext}(x)} \tag{4}$$

To achieve the maximum power, the external load $(R_{a,ext}(x))$ should be equal to the internal resistance, therefore, the space-dependent power density is given by

$$P_{d,\max}(x) = \frac{1}{2}j(x)^2R_{a,cell}(x) \tag{5}$$

The total maximum power output is

$$P_{\max} = W\int_0^L P_d(x)dx \tag{6}$$

where W and L are, respectively, the width and length of the RED membrane.

Due to the flow characteristics in the micro channel, the pump consumed could not be ignored. According to Ref. [39], the pressure drop over the single HC and LC channels are [8].

$$dp_H = \frac{12\mu_H V_H dx}{W\delta_H^3}, dp_L = \frac{12\mu_L V_L dx}{W\delta_L^3} \tag{7}$$

where V_H and V_L are the volume flowrates of the HC and LC solutions with the viscosity being $\mu_H$and μ_L respectively. The relation of the viscosity and NaCl concentration can be found in Refs. [40,41]. The total pump consumed can be calculated as

$$P_{pum} = \int_o^L N\zeta\left(\frac{6\mu_H V_H^2}{W\delta_H^3}+\frac{6\mu_L V_L^2}{W\delta_L^3}\right)dx \tag{8}$$

where$\zeta$is a correlation factor concerning the geometric effects [38].

Therefore, the net power output is

$$P_{RED} = P_{\max} - P_{pum} \tag{9}$$

Furthermore, the energy efficiency of the RED stack, indicating the ratio of the power actual extracted and the energy that could be extracted in the reversible process, can be defined as

$$\eta_{RED} = P_{RED}/\Delta G_{RED} \tag{10}$$

where ΔG_{RED} is the maximum potential that can be transformed into electricity in the RED stack, which can be expressed as [42].

$$\Delta G_{RED} = 2RT\left[V_H C_H \ln\frac{C_H}{C_T} + V_L C_L \ln\frac{C_L}{C_T}\right] \tag{11}$$

where $C_T$is the concentration of the mixed concentrated and diluted solutions.

2.2. Salt and water transfer through the membranes

For simplicity, some assumptions are made to model the RED process: (1) The concentration polarization both on the HC side and LC side are ignored. (2) The ions carried by the transmembrane water flux are not included. (3) The diffusion coefficients for the water and ions are constant.

Salt transport from the high concentration electrolyte to the low concentration electrolyte is composed of a Coulombic part and a part due to co-ion transport [38]:

$$J_i(x) = J_{Coul,i}(x) + J_{cit,i}(x) = \frac{t_i j(x)}{F} + \frac{2D_i}{\delta_m}[C_H(x) - C_L(x)] \tag{12}$$

where$t$is the ion transport number and i refers to Na^+ or Cl^-.

Opposite to the salt flux, there is a water flux (J_{water}) due to osmosis of water from the LC solution to the HC solution compartment [43].

$$J_{water}(x) = -\frac{2D_{Water}}{\delta_m}[C_H(x) - C_L(x)] \tag{13}$$

As depicted in Fig. 2, in the HC compartment, the total mass change stems from the sum of the mass decrease of the NaCl and increase of the water due to the osmic effect.

$$\frac{d[V_H(x)\rho_H(x)]}{dx} = -WJ_{NaCl}(x)M_{NaCl} + WJ_{water}(x)M_{H_2O} \tag{14}$$

where ρ_H is the density of the HC solution. Meanwhile, the mass conservation of NaCl reads

$$\frac{d[V_H(x)C_H(x)]}{dx} = -WJ_{NaCl}(x) \tag{15}$$

Similarly, in the LC compartment, the mass increase origins from the NaCl mass transfer from the HC compartment and the water due to the osmic effect.

$$\frac{d[V_L(x)\rho_L(x)]}{dx} = WJ_{NaCl}(x)M_{NaCl} - WJ_{water}(x)M_{H_2O} \tag{16}$$

where $\rho_L$is the density of the LC solution. Meanwhile, the mass conservation of NaCl reads

$$\frac{d[V_L(x)C_L(x)]}{dx} = WJ_{NaCl}(x) \tag{17}$$

The concentration dependent density (ρ) of the NaCl-water mixture can be found in the appendix.

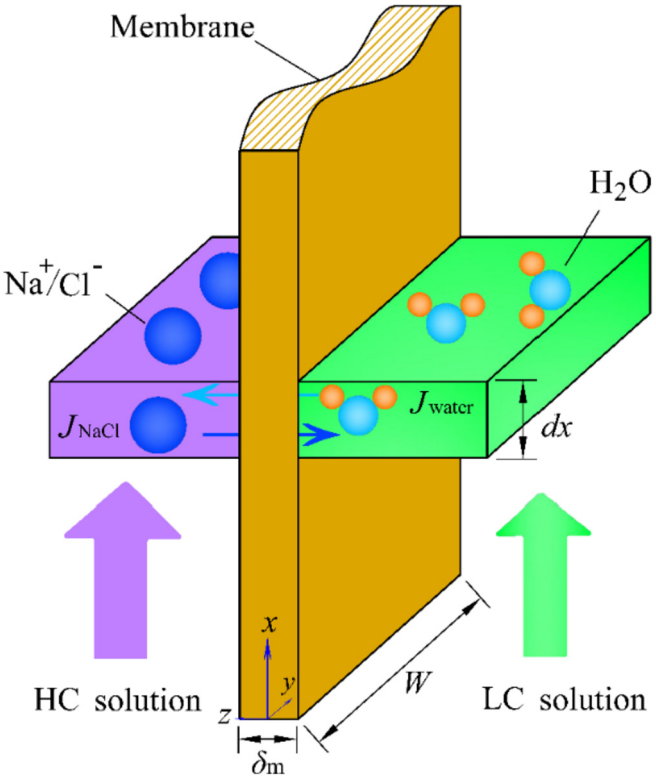

Fig. 2. Mass conservation along the flow direction in an infinitesimal length.

The distributions of the concentrations ($C_H(x)$ and $C_L(x)$) and volume flowrates ($V_H(x)$ and $V_L(x)$) in the HC and LC compartments by solving Eqs. (14)–(17), with the boundary conditions (the inlet volume flow rate and concentration of the HC and LC solutions) given by

$$C_H(0) = C_{H,in}, V_H(0) = V_{H,in}, \tag{18}$$

$$C_L(0) = C_{L,in}, V_L(0) = V_{L,in}, \tag{19}$$

3. The impact of flow rates on the performance of the RED stack

3. .1Model validation

The model presented in this paper is validated by the measured values of small Qianqiu homogen stack of 25 cells [38] and Fumasep FAD/FKD stack of 50 cells [44]. The obstruction factor describing the extra electrical resistance of the water compartments induced by the spacer is 1.7 for Qianqiu stack and 1.72 for Fumasep stack. The spacer thickness is $\delta_H = \delta_L = 200\mu m$. The input NaCl concentrations are 512.8 mol/m^3 for the HC compartment and 17.1 mol/m^3 for the LC compartment, respectively. The model studied in this paper can be justified by good accordance between the results calculated and experimental measured data as show in Fig. 3.

3.2. Sensitivity analysis

To give a first impression of the behavior with the different HC and LC flow rates in a RED cell, the model is used to simulate a 50 cell stack (10cm × 10cm), equipped with Qianqiu homogen. The membrane properties can be found in Table 1. The spacer thickness

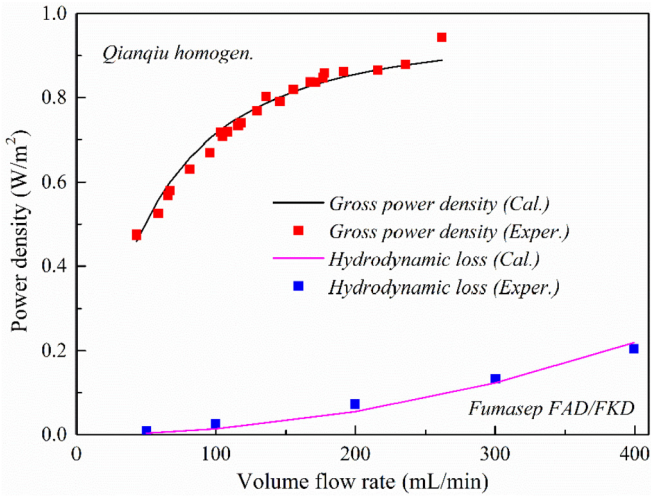

Fig. 3. Validation of the model. Calculated (line) and measured (square points) power densities of small Qianqiu honogen of 25 cells and small Fumasep FAD/FKD of 50 cells as a function of the volume flow rate. The spacer thickness (both compartments) for the RED stack is $\delta_H = \delta_L = 200\mu m$. The input NaCl concentrations are 512.8 mol/m^3 for the HC compartment and 17.1 mol/m^3 for the LC compartment, respectively. The input volume flow rates of the HC and LC compartments are equal.

is $\delta_H = \delta_L = 200\mu m$. The obstruction factor is 1.96. The input NaCl concentrations are 512.8 mol/m^3 for the HC compartment and 17.1 mol/m^3 for the LC compartment, respectively. The detailed prescribed parameters are listed in Table 2. Fig. 4 shows the gross power density, net power density, and hydrodynamic loss of small Qianqiu stacks of 50 cells as a function of the inlet volume flow rates of the HC and LC solutions. The gross power density and hydrodynamic loss both increase with increasing inlet volume flowrates of the solutions based on the fact that for a RED cell with given size, larger volume flowrates lead to more slow variation of the concentration in for both the HC and LC solutions, thus a higher cell potential based on Eq. (1). And according to Eq. (8), the larger volume flowrate, the larger value of the hydrodynamic loss, which increases dramatically at higher volume flowrates, as shown in Fig. 4. Therefore, the net power output (difference between the gross power density and the hydrodynamic loss) increase first, then decreases with increasing inlet volume flowrates of the HC and LC solutions, respectively. There exist optimal HC and LC volume flowrates leading to the maximum value of the net power density. The optimal HC flowrate is much less than the optimal LC flowrate as the hydrodynamic loss increases with increasing HC flowrate more rapidly than LC flow rate as shown in Fig. 4, which is in accord with Ref. [27], where this phenomenon has been experimentally examined. Furthermore, as depicted in Fig. 5, the energy efficiency decreases with increasing inlet volume flowrates of the HC and LC compartments based on the fact that the Gibbs free energy of the solutions can be utilized more adequately at lower volume flow rates for a limited membrane area. As the net power density and energy efficiency are main important criteria evaluating the RED performance, in some actual applications, the above two figure of merits should be both considered. However, they could not achieve their maximum values simultaneously as shown in Fig. 5.

4. Performance optimization

Multi-objective optimization is widely adopted to coordinate the conflicting performance specifications, whose results are usually a set of non-dominated solutions (Pareto frontier) with minimum conflict between the objectives under the multi-

Table 1
Membrane properties [47,48].

Membrane	δ_m(μm)	$R(\Omega \cdot cm^{-2})$		α(%)		$D_{Nacl}(m^2/s)$	$D_{water}(m^2/s)$
		AEM	CEM	AEM	CEM		
Qianqiu homogen	250	2.85	1.97	0.863	0.82	3.2E-11	7.9E-9
Qianqiu heterogen	580	2.85	1.97	0.863	0.82	2E-11	3.9E-9
Fumasep FAD/FKD	80	0.89	0.89	0.86	0.86	1.3E-11	1.3E-9
Neosepta AMX/CMX	150	2.35	2.91	0.907	0.99	5.5E-11	5.8E-10
Selemion AMV/CMV	120	3.15	2.29	0.873	0.988	3.1E-12	1.2E-10

Table 2
Prescribed parameters of the RED system.

Parameters	Notation	Value
Operating temperature [K]	T	293.15
Effective hydrated ion radius for Na^+ [pm]	A_{Na^+}	450
Effective hydrated ion radius for Cl^- [pm]	A_{Cl^-}	300
Faraday constant [C/mol]	F	96485
Gas constant [$J \cdot mol^{-1} \cdot K^{-1}$]	R	8.314
Molar conductivity for the HC solution [$S \cdot m^2 \cdot mol^{-1}$]	$\Lambda_{m,H}$	0.009219
Molar conductivity for the LC solution [$S \cdot m^2 \cdot mol^{-1}$]	$\Lambda_{m,L}$	0.0117

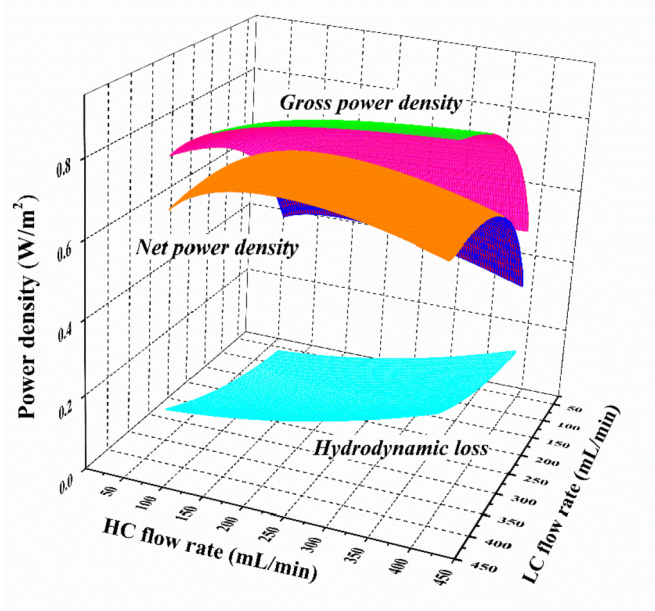

Fig. 4. Gross power density, net power density, and hydrodynamic loss of small Qianqiu stacks of 50 cells as a function of the inlet volume flow rates of the HC and LC compartments.

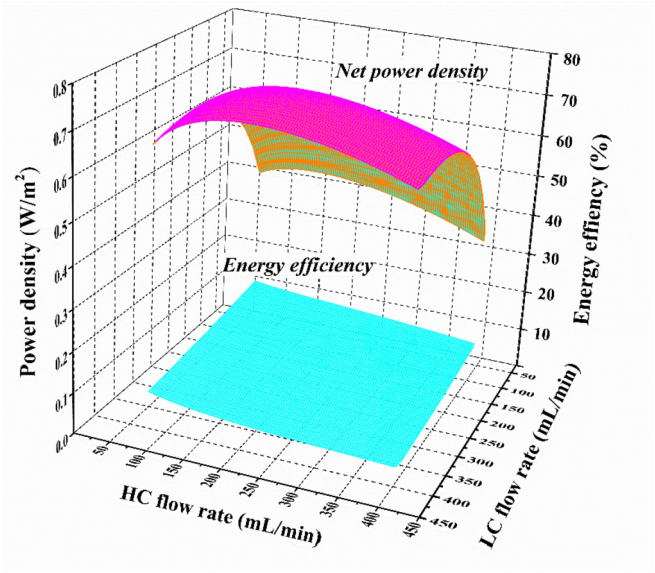

Fig. 5. Net power density, and energy efficiency of small Qianqiu stacks of 50 cells as a function of the inlet volume flow rates of the HC and LC compartments.

objective algorithms such as NSGA-II [37]. As each point in the Pareto frontier represents certain weights of the objectives. Therefore, to select the final optimal point, decision-making techniques should be employed, such as LINMAP, TOPSIS, and Belman–Zadeh methods [45], among which the TOPSIS is widely applied, indicating the maximum deviation from the non-ideal point and a minimum deviation from the ideal point. As mentioned above, to optimize a RED system, the energy efficiency and net power density could not achieve their maximum value simultaneously. The energy efficiency evaluates the degree of utilization of the Gibbs free energy of the concentrated and diluted solutions, and the net power density is the criterion measuring how much we get from these solutions. In this study, an optimization based on NSGA-II has been conducted to achieve an appropriate compromise between the energy efficiency and the net power density. The flow chart for the calculation is depicted in Fig. 6. In the calculations, for a given membrane, the range of inlet volume flow rates is between 50 mL/min to 700 mL/min to cover the optimal volume flowrates under the maximum net power density and maximum energy efficiency.

4.1. Pareto frontier and the final optimal point

Fig. 7 depicts the Pareto frontier calculated through the multi-objective optimization for a 50 cell RED system with different membranes listed in Table 1, which illustrates the obvious repugnant phenomenon of the maximum energy efficiency and net power density. As each point in the Pareto frontier represents certain weights of the two conflicting objectives, the top-left point represents the energy efficiency is mostly weighted, corresponding to the single objective optimization for energy efficiency, whereas the bottom-right indicates the net power density is

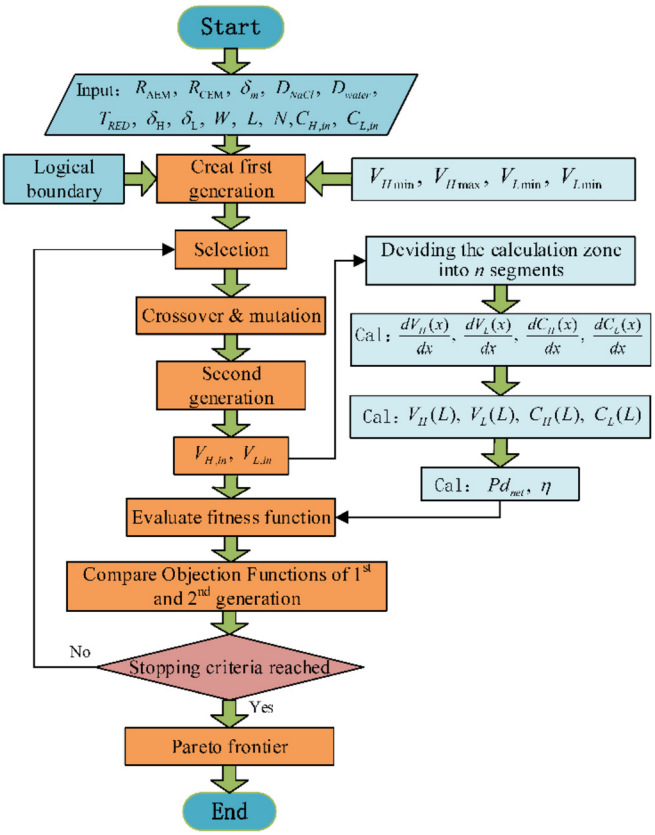

Fig. 6. Calculation flow chart for the multi-objective optimization.

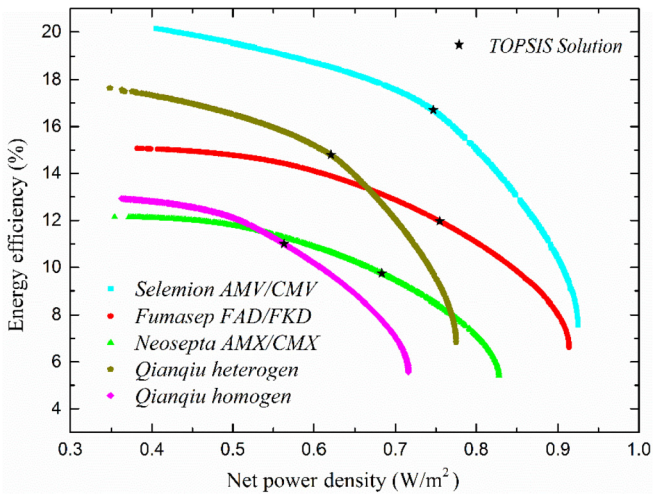

Fig. 7. Pareto frontier from multi-objective optimization of the RED system with different membranes. The star-marked points are obtained by the TOPSIS algorithm.

mostly weighted, in accord with the situation under the single objective optimization for net power density. Selemion AMV/CMV could lead to larger values of maximum net power density and maximum energy efficiency. The star-marked point represent the final optimal one selected by the TOPSIS algorithm. For a prescribed membrane, under the multi-objective optimization, the net power density and exergy efficiency exhibit moderate values, as shown in Fig. 7.

4.2. Performance under the optimal conditions

For a better illustration on the performance of the RED system under the multi-objective optimization, the gross power density, net power density and energy efficiency under the corresponding single-objective optimization methods were calculated and compared. The profiles of the volume flowrate and concentrations along the flow direction under different optimization methods are plotted in Fig. 8. In the previous models, the volume flow rates in the HC and LC compartments are treated constant during the mass transfer processes. However, in present model, the changes of volume flowrate are considered, as depicted in Fig. 8(a) and (b), where the flow rate of the HC solution increases along the flow direction while that of the LC solution decreases. The changes of the volume flow rate originate from the transmembrane water flux from the LC solution to the HC solution induced by osmosis effects, thus to bring an augment of the HC solution volume flow rate. Under the optimal conditions under the multi-objective optimization, the volume flow rate of the HC compartment is much less than that of the LC compartment. However, the optimal flow rates of the HC and LC solutions are nearly the same under the optimization for energy efficiency. Compared to the optimal values of volume flow rates under the single objective optimizations for net power density and energy efficiency, the optimal flow rates under the multi-objective optimization exhibit moderate values.

The concentrations of the HC and LC solutions along the flow direction under three different optimization methods are plotted in Fig. 8 (c) and (d). Under the maximum net power density, the concentration changes much slowly than those under the other two optimization methods due to the relative larger volume flow rates. However, the concentration changes dramatically under the maximum energy efficiency, due to the small volume flow rates that make the final concentration approach more close to the mixed one, thus to induce a higher energy efficiency, based on Eq. (11). The concentration derivation of the LC solution under the multi-objective optimization is a little more than that under the maximum net power density. But the concentration for the HC solution along the flow direction drops much more obviously, resulting a larger energy efficiency than that under the maximum net power density.

Fig. 9 (a) demonstrates the power densities and hydrodynamic loss under the multi-objective optimization. As the relative small change of the flow rates of the HC and LC solutions, according to Eq. (8), the density of hydrodynamic loss nearly stays unchanged in the flow direction, which can also be observed in Fig. 9 (c). The gross power density first increases, reaches its maximum value, then decreases along the flow direction. Near the inlet region, although the Nernst potential is highest, the ohmic resistance is the highest due to the lowest concentration of the LC compartment, thus the gross power density is not the highest. As the developing of the RED process, the decrease magnitude of the Nernst potential difference is lower than that of the ohmic resistance, therefore, the gross power density increases. As the RED process develops further, the Nernst potential difference decreases much sharped due to the decrease of the NaCl concentration of the HC solution and increase of the NaCl concentration of the LC solution, the gross power density decreases. Therefore, there a maximum value of the gross power density along the flow direction. As the density of hydrodynamic loss nearly stays unchanged in the flow direction, the net power density (the difference of the electrical power density and the hydrodynamic loss) displays the same trend as the gross power density.

In Fig. 9 (b), the profiles of gross power density under different optimization objectives are presented. Under the maximum net power density, the gross power density changes relatively slowest.

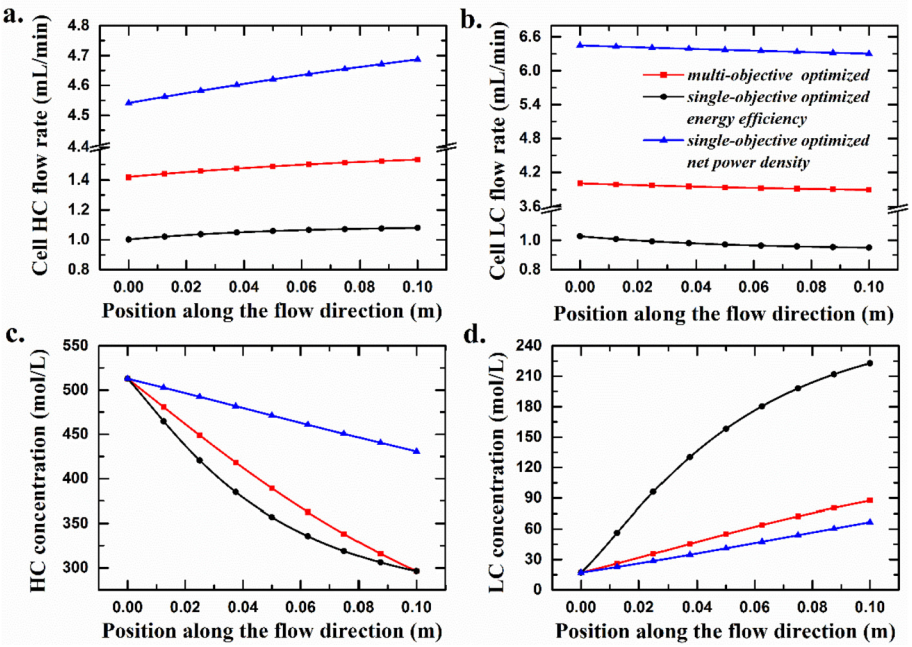

Fig. 8. Profiles of volume flow rate and concentration along the flow direction in the HC and LC compartments under different optimization methods for a 50 cell stack with Fumasep FAD/FKD.

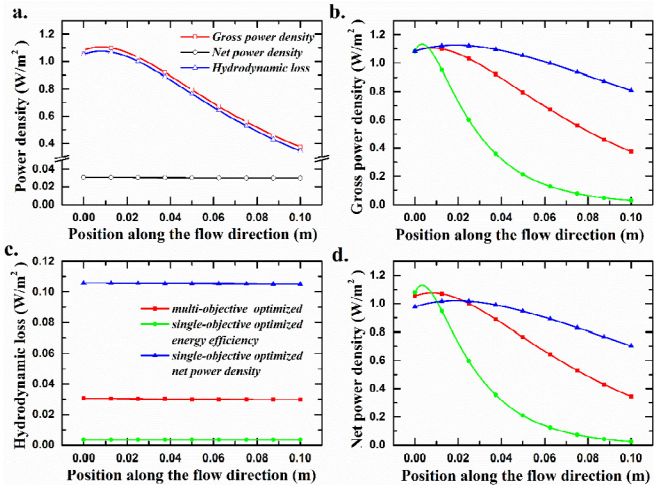

Fig. 9. Profiles of power density and hydrodynamic loss along the flow direction in the HC and LC compartments under different optimization objectives for a 50 cell stack with Fumasep FAD/FKD. Furthermore, the gross power density, net power density and the hydrodynamic loss along the flow direction under the multi-objective optimization is plotted together (see Fig. 9 (a)).

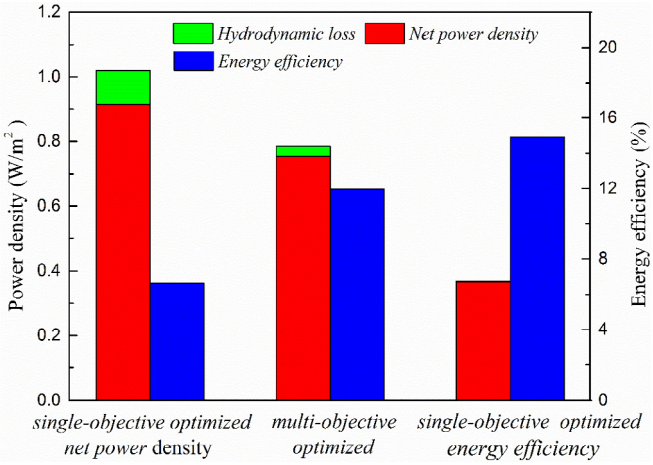

Fig. 10. Comparison of power density under different optimization objectives for a 50 cell stack with Fumasep FAD/FKD.

While under the maximum energy efficiency, the gross power density changes dramatically along the flow direction, which means the highest utilization of the Gibbs free energy of the solutions. As shown in Fig. 8, the optimal flow rates of the HC and LC solutions under the maximum net power density are the largest, resulting in the largest hydrodynamic loss, as depicted in Fig. 9 (c). The profiles of net power density are present in Fig. 9 (d), which presents the same characteristics of the gross power density shown in Fig. 9 (c) because of the nearly unchanged hydrodynamic loss along the flow direction. Due to the smallest hydrodynamic loss obtained under single objective optimization for energy efficiency, the net power density under the maximum energy efficiency at the inlet region are the largest. As the multi-objective optimization coordinates both the energy efficiency and net power density, the profiles present moderate behaviors.

Table 3
Performance comparisons under different optimization methods.

Membrane	multi-objective optimization compared to single-objective optimization (maximum P_{net})		multi-objective optimization compared to single-objective optimization (maximum η)	
	P_{net}	η	P_{net}	η
Qianqiu homogen	−21.33%	+97.81%	+55.32%	−14.88%
Qianqiu heterogen	−19.94%	+116.17%	+77.99%	−16.12%
Fumasep FAD/FKD	−17.39%	+81.03%	+97.77%	−20.60%
Neosepta AMX/CMX	−17.49%	+79.51%	+93.10%	−19.83%
Selemion AMV/CMV	−19.24%	+120.41%	+84.22%	−17.10%

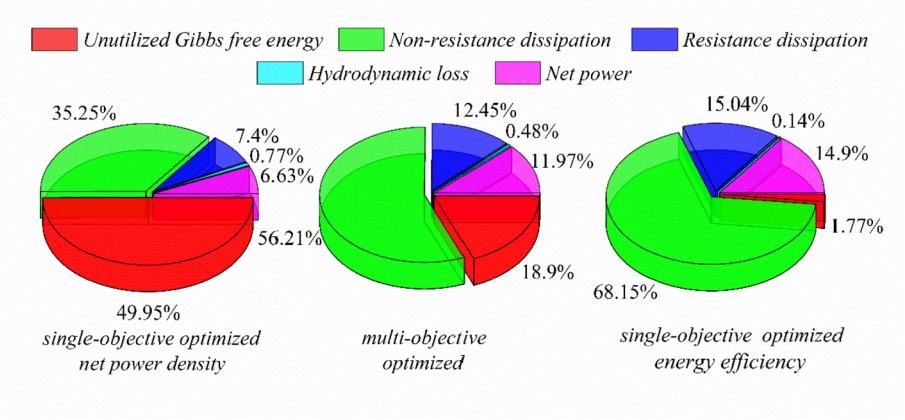

Fig. 11. Energy utilization specifications under different optimization objectives for a 50 cell stack with Fumasep FAD/FKD.

The average net power density and the hydrodynamic loss are depicted in Fig. 10. Compared with the performance under the single-objective optimization for net power density, the net power density under the multi-objective optimization was reduced by only 17.39%, but the energy efficiency increased by 81.03%. Compared with the performance under the single-objective optimization for energy efficiency, the energy efficiency under the multi-objective optimization was reduced by only 20.60%, but the net power density increased by 97.77%. What's more, compared with the performance under the single-objective optimization for net power density, the hydrodynamic loss is much reduced under the multi-objective optimization. More comparisons with varied membranes are listed in Table 3.

The energy utilization specifications under different optimization objectives are presented in Fig. 11. Under the optimization for maximum net power density, the energy efficiency is only 6.63%, most of the energy (Gibbs free energy of the outlet of the RED stacks) are evacuated. Then comes by the non-resistance dissipation. Under the optimization for maximum energy efficiency, the energy efficiency reaches 14.9%. The unutilized takes only 1.77%, due to the sufficient ion transfer through the membrane, meanwhile the non-resistance dissipation approaches 68.15% which comes from the irreversibility during the mass transfer process. Under the multi-objective optimization, the energy efficiency reaches 11.97% and the energy unutilized is 18.9%. Therefore, to maintain more net power output, the volume flow rates should be at reasonable large values, which results in increased percentage of unutilized energy and decreased non-resistance dissipation, meanwhile the energy efficiency is lowered. Moreover, the non-resistance dissipation mainly originates from the osmic effect, co-ion transport and the imperfect selectivity of the IEMs. Therefore, a qualified membrane with high performance is appealing to improve the performance of the RED stacks.

5. Conclusions

In this paper, we have proposed a refined model to describe the RED process by considering the osmic transmembrane water flux, therefore the volume flow rates of the HC and LC solutions vary along the flow direction, which is more close to the actual RED process. In addition, the concentration depended density and viscosity are also taken into account. The model was justified by good accordance between the results calculated and experimental measured data. Results revealed that there exist optimal flowrates of the HC and LC solutions leading to the maximum net power density, however the energy efficiency achieves its maximum value at lower flowrates due to more sufficient ion transfer through the membranes. To achieve such a compromise between the maximum net power density and maximum energy efficiency. An optimization based on NSGA-II was conducted to obtain the Pareto frontiers of the RED system with different membranes. And the TOPSIS decision-making method was used to choose the final optimum point. Besides, the net power output and energy efficiency under single-objective optimization methods were calculated and compared. For a specified 50 cell stack with Fumasep FAD/FKD, compared with the performance under the single-objective optimization for net power density, the net power density under the multi-objective optimization was reduced by only 17.39%, but the energy efficiency increased by 81.03%. Compared with the performance under the single-objective optimization for energy efficiency, the energy efficiency under the multi-objective optimization was reduced by only 20.60%, but the net power density increased by 97.77%. The operation parameters obtained by the multi-objective optimization can balance both the power density and energy efficiency of the RED system, thus to serve as a guidance for designing and running actual RED stacks for actual applications.

Acknowledgments

We acknowledge the support received from the National Natural Science Foundation of China (51706076, 51736004).

Nomenclature

A	Effective hydrated ion radius (pm)
C	Electrolyte concentration (in molality) ($mol \cdot kg^{-1}$)
D_{NaCl}, D_{Water}	Diffusion constants of NaCl and water, respectively ($m^2 \cdot s^{-1}$)
E_{cell}	Electromotive force of one cell (V)
F	Faraday constant ($96485C \cdot mol^{-1}$)
f	Obstruction factor
ΔG	Maximum potential that can be transformed into electricity in the RED stack (W)
I	Ion strength of a solution ($mol \cdot L^{-1}$)
J	Molar flux ($mol \cdot s^{-1} \cdot m^{-2}$)
j	Current density ($A \cdot m^2$)
M_{H_2O}	Mole mass H_2O ($0.01802kg \cdot mol^{-1}$)
N	Cell number
P	Power (W)
P_d	Power density (W/m^2)
p_H, p_L	Pressure over the single HC and LC channels, respectively (Pa)

R	Gas constant ($8.314 J \cdot mol^{-1} \cdot K^{-1}$)
R_{el}	electrode area ohmic resistance ($\Omega \cdot m^2$)
R_{AEM}, R_{CEM}	Area resistance of the AEM and CEM, respectively ($\Omega \cdot m^2$)
T	Temperature (K)
V	Volume flow rate ($m^3 \cdot s^{-1}$)
W, L	Width and length of the RED membrane (m)
x	Axial position along the RED module (m)
z	Valency of an ion

Greek Symbols

α	Permselectivity of the ion-selective membrane
γ	Activity coefficient
μ	Viscosity ($kg \cdot m^{-1} \cdot s^{-1}$)
δ_m	Membrane thickness (m)
$\delta_H \delta_L$	Thickness of the HC and LC solution compartment, respectively (m)
η	Efficiency
Λ_m	Molar conductivity ($S \cdot m^2 \cdot mol^{-1}$)
ρ	Density ($kg \cdot m^{-3}$)

Subscripts

H	High concentration
L	Low concentration
ext	External load
app	Apparent
max	Maximum

Abbreviations

HC	High concentration
LC	Low concentration
RED	Reversed electrodialysis
PRO	Pressure retarded osmosis
CAPMIX	Capacitive mixing
MRC	Microbial reverse-electrodialysis cell
CEM	Cation-exchange membrane
AEM	Anion-exchange membrane

Appendix

The density (ρ) of the NaCl-water mixture can be calculated as [46]

$$\rho = \frac{1}{\frac{\omega_{H_2O}}{\rho_{H_2O}} + \frac{\omega_{NaCl}}{\rho_{app,NaCl}}} \tag{20}$$

where ω_{H_2O} and ω_{NaCl} are the mass fractions of water and NaCl, andρ_{H_2O} is the density of water, $\rho_{app,NaCl}$is the apparent density of NaCl, which can be written as

$$\rho_{app,NaCl} = \frac{(c_0 \omega_{NaCl} + c_1)\exp\left(0.000001(t + c_4)^2\right)}{\omega_{NaCl} + c_2 + c_3 t} \tag{21}$$

where t is the temperature in °C. For NaCl aqueous solution, the parameters ($c_0 - c_4$) can be found in Ref. [46].

References

[1] Long R, Bao YJ, Huang XM, Liu W. Exergy analysis and working fluid selection of organic Rankine cycle for low grade waste heat recovery. Energy 2014;73(7):475–83.
[2] Long R, Li B, Liu Z, Liu W. A hybrid system using a regenerative electrochemical cycle to harvest waste heat from the proton exchange membrane fuel cell. Energy 2015;93:2079–86.
[3] Long R, Li B, Liu Z, Liu W. Performance analysis of a solar-powered solid state heat engine for electricity generation. Energy 2015;93:165–72.
[4] Long R, Li B, Liu Z, Liu W. Performance analysis of a solar-powered electrochemical refrigerator. Chem Eng J 2016;284:325–32.
[5] Hickenbottom KL, Vanneste J, Cath TY. Assessment of alternative draw solutions for optimized performance of a closed-loop osmotic heat engine. J Membr Sci 2016;504:162–75.
[6] Achilli A, Childress AE, Cath TY. Power generation with pressure retarded osmosis: an experimental and theoretical investigation. J Membr Sci 2009;343(1–2):42–52.
[7] Mcginnis RL, Mccutcheon JR, Elimelech M. A novel ammonia–carbon dioxide osmotic heat engine for power generation. J Membr Sci 2007;305(1–2):13–9.
[8] Vermaas DA, Saakes M, Nijmeijer K. Power generation using profiled membranes in reverse electrodialysis. Fuel Energy Abstr 2011;385–386:234–42.
[9] Güler E, Elizen R, Saakes M, Nijmeijer K. Micro-structured membranes for electricity generation by reverse electrodialysis. J Membr Sci 2014;458(6):136–48.
[10] Weiner AM, Mcgovern RK, John HLV. A new reverse electrodialysis design strategy which significantly reduces the levelized cost of electricity. J Membr Sci 2015;493:605–14.
[11] Tufa Ramato A, Curcio E, Brauns E, van Baak W, Fontananova E, Di Profio G. Membrane distillation and reverse electrodialysis for near-zero liquid discharge and low energy seawater desalination. J Membr Sci 2015;496:325–33.
[12] Rica RA, Ziano R, Salerno D, Mantegazza F, Bazant MZ, Brogioli D. Electrodiffusion of ions in porous electrodes for capacitive extraction of renewable energy from salinity differences. Electrochim Acta 2013;92(1):304–14.
[13] Liu F, Schaetzle O, Sales BB, Saakes M, Buisman CJN, Hamelers HVM. Effect of additional charging and current density on the performance of Capacitive energy extraction based on Donnan Potential. Energy Environ Sci 2012;5(9):8642–50.
[14] Brogioli D, Ziano R, Rica A, Salerno R,D, Kozynchenko O, Hamelers M, HV, et al. Exploiting the spontaneous potential of the electrodes used in the capacitive mixing technique for the extraction of energy from salinity difference. Energy Environ Sci 2012;5(12):9870–80.
[15] Rica RA, Ziano R, Salerno D, Mantegazza F, Brogioli D. Thermodynamic relation between voltage-concentration dependence and salt adsorption in electrochemical cells. Phys Rev Lett 2012;109(15):684–91.
[16] Long R, Li B, Liu Z, Liu W. Hybrid membrane distillation-reverse electrodialysis electricity generation system to harvest low-grade thermal energy. J Membr Sci 2017;525:107–15.
[17] Tedesco M, Cipollina A, Tamburini A, Wv Baak, Micale G. Modelling the Reverse ElectroDialysis process with seawater and concentrated brines. Desalination Water Treat 2012;49(1):404–24.
[18] Veerman J, Saakes M, Metz S, Harmsen G. Reverse electrodialysis: a validated process model for design and optimization. Chem Eng J 2011;166(1):256–68.
[19] Tedesco M, Cipollina A, Tamburini A, van Baak W, Micale G. Modelling the Reverse ElectroDialysis process with seawater and concentrated brines. Desalination Water Treat 2012;49(1–3):404–24.
[20] Veerman J, Post J, Saakes M, Metz S, Harmsen G. Reducing power losses caused by ionic shortcut currents in reverse electrodialysis stacks by a validated model. J Membr Sci 2008;310(1):418–30.
[21] Kim KS, Ryoo W, Chun MS, Chung GY. Simulation of enhanced power generation by reverse electrodialysis stack module in serial configuration. Desalination 2013;318(10):79–87.
[22] Jeong HI, Kim HJ, Kim DK. Numerical analysis of transport phenomena in reverse electrodialysis for system design and optimization. Energy 2014;68(4):229–37.
[23] Kang BD, Kim HJ, Lee MG, Kim DK. Numerical study on energy harvesting from concentration gradient by reverse electrodialysis in anodic alumina nanopores. Energy 2015;86:525–38.
[24] Gurreri L, Tamburini A, Cipollina A, Micale G, Ciofalo M. CFD prediction of concentration polarization phenomena in spacer-filled channels for reverse electrodialysis. J Membr Sci 2014;468:133–48.
[25] Pawlowski S, Crespo JG, Velizarov S. Pressure drop in reverse electrodialysis: experimental and modeling studies for stacks with variable number of cell pairs. J Membr Sci 2014;462:96–111.
[26] Geise GM, Curtis AJ, Hatzell MC, Hickner MA, Logan BE. Salt concentration differences alter membrane resistance in reverse electrodialysis stacks. Environ Sci Technol Lett 2013;1(1):36–9.
[27] Zhu X, He W, Logan BE. Reducing pumping energy by using different flow rates of high and low concentration solutions in reverse electrodialysis cells. J Membr Sci 2015;486:215–21.
[28] Hong JG, Zhang W, Luo J, Chen Y. Modeling of power generation from the mixing of simulated saline and freshwater with a reverse electrodialysis system: the effect of monovalent and multivalent ions. Appl Energy 2013;110:244–51.
[29] Kim J, Kim SJ, Kim D-K. Energy harvesting from salinity gradient by reverse electrodialysis with anodic alumina nanopores. Energy 2013;51:413–21.
[30] Güler E, Elizen R, Vermaas DA, Saakes M, Nijmeijer K. Performance-determining membrane properties in reverse electrodialysis. J Membr Sci 2013;446:266–76.
[31] Güler E, Elizen R, Saakes M, Nijmeijer K. Micro-structured membranes for electricity generation by reverse electrodialysis. J Membr Sci 2014;458:136–48.
[32] Jin GH, Chen Y. Nanocomposite reverse electrodialysis (RED) ion-exchange membranes for salinity gradient power generation. J Membr Sci

2014;460(12):139–47.
[33] Vermaas DA, Saakes M, Nijmeijer K. Power generation using profiled membranes in reverse electrodialysis. J Membr Sci 2011;385:234–42.
[34] Liu J, Geise GM, Luo X, Hou H, Zhang F, Feng Y, et al. Patterned ion exchange membranes for improved power production in microbial reverse-electrodialysis cells. J Power Sources 2014;271:437–43.
[35] Luo X, Nam JY, Zhang F, Zhang X, Liang P, Huang X, et al. Optimization of membrane stack configuration for efficient hydrogen production in microbial reverse-electrodialysis electrolysis cells coupled with thermolytic solutions. Bioresour Technol 2013;140C(3):399–405.
[36] Chen X, Li W, Gong G, Wan Z, Tu Z. Parametric analysis and optimization of PEMFC system for maximum power and efficiency using MOEA/D. Appl Therm Eng 2017;121:400–9.
[37] Long R, Li B, Liu Z, Liu W. Multi-objective optimization of a continuous thermally regenerative electrochemical cycle for waste heat recovery. Energy 2015;93:1022–9.
[38] Veerman J, Saakes M, Metz SJ, Harmsen GJ. Reverse electrodialysis: a validated process model for design and optimization. Chem Eng J 2011;166(1):256–68.
[39] Vermaas DA, Saakes M, Nijmeijer K. Doubled power density from salinity gradients at reduced intermembrane distance. Environ Sci Technol 2011;45(16):7089–95.
[40] Laliberté M. Erratum: model for calculating the viscosity of aqueous solutions. J Chem Eng Data 2007;52:321–35.
[41] Laliberté M. Model for calculating the viscosity of aqueous solutions. J Chem Eng Data 2007;52(52):321–35.
[42] Sadeghian RB, Pantchenko O, Tate D, Shakouri A. Miniaturized concentration cells for small-scale energy harvesting based on reverse electrodialysis. Appl Phys Lett 2011;99(17):173702–3.
[43] Veerman J, De Jong R, Saakes M, Metz S, Harmsen G. Reverse electrodialysis: comparison of six commercial membrane pairs on the thermodynamic efficiency and power density. J Membr Sci 2009;343(1):7–15.
[44] Veerman J, Saakes M, Metz SJ, Harmsen GJ. Reverse electrodialysis: performance of a stack with 50 cells on the mixing of sea and river water. J Membr Sci 2009;327(1–2):136–44.
[45] Güler E, Elizen R, Vermaas DA, Saakes M, Nijmeijer K. Performance-determining membrane properties in reverse electrodialysis. J Membr Sci 2013;446(11):266–76.
[46] Veerman J, Jong RMD, Saakes M, Metz SJ, Harmsen GJ. Reverse electrodialysis: comparison of six commercial membrane pairs on the thermodynamic efficiency and power density. J Membr Sci 2009;343(1):7–15.
[47] Ahmadi P, Rosen MA, Dincer I. Multi-objective exergy-based optimization of a polygeneration energy system using an evolutionary algorithm. Energy 2012;46(1):21–31.
[48] And ML, Cooper WE. Model for calculating the density of aqueous electrolyte solutions. ChemInform 2004;35(47):1141–51.